

# Diffusive–Nondiffusive Flux Decompositions in Atmospheric Boundary Layers

TOMAS CHOR,<sup>a</sup> JAMES C. MCWILLIAMS, AND MARCELO CHAMECKI<sup>b</sup>

*University of California, Los Angeles, Los Angeles, California*

(Manuscript received 25 March 2020, in final form 24 June 2020)

**ABSTRACT:** Eddy diffusivity models are a common method to parameterize turbulent fluxes in the atmospheric sciences community. However, their inability to handle convective boundary layers leads to the addition of a nondiffusive flux component (usually called nonlocal) alongside the original diffusive term (usually called local). Both components are often modeled for convective conditions based on the shape of the eddy diffusivity profile for neutral conditions. This assumption of shape is traditionally employed due to the difficulty of estimating both components based on numerically simulated turbulent fluxes without any a priori assumptions. In this manuscript we propose a novel method to avoid this issue and estimate both components from numerical simulations without having to assume any a priori shape or scaling for either. Our approach is based on optimizing results from a modeling perspective and taking as much advantage as possible from the diffusive term, thus maximizing the eddy diffusivity. We use our method to diagnostically investigate four different large-eddy simulations spanning different stability regimes, which reveal that nondiffusive fluxes are important even when trying to minimize them. Furthermore, the calculated profiles for both diffusive and nondiffusive fluxes suggest that their shapes change with stability, which is an effect that is not included in most models currently in use. Finally, we use our results to discuss modeling approaches and identify opportunities for improving current models.

**KEYWORDS:** Fluxes; Mass fluxes/transport; Turbulence; Convective parameterization; Large eddy simulations; Tracers

## 1. Introduction

In the atmospheric sciences community, eddy diffusivity models have been invaluable when representing turbulent fluxes (Ghannam et al. 2017). The premise in these models is that the action of eddies can be parameterized as a diffusive process via a flow-dependent eddy diffusivity. This approach [hereafter referred to as gradient transport models (GTM) but also known as  $K$  theory; Stull 1988] can be written as

$$\langle w'c' \rangle = -K(z) \frac{\partial \langle C \rangle}{\partial z}, \quad (1)$$

where  $C$  is the concentration of a passive tracer,  $K(z)$  is the eddy diffusivity of the flow, and the brackets denote an average over homogeneous dimensions.

To justify GTMs from a theoretical perspective, it is necessary that the eddies be smaller than some characteristic length scale over which the mean gradient of the transported quantity profiles do not change appreciably (Corrsin 1975). Thus, Eq. (1) can be formally justified for neutral atmospheric boundary layers (ABLs), where the eddies are relatively small (Moeng and Sullivan 1994; Stull 1988), but should not be expected to hold for convective ABLs which have large convective plumes (also called thermals; Hunt et al. 1988; Williams and Hacker 1993). If we calculate the eddy diffusivity  $K$  from observations of turbulent fluxes and mean gradient profiles in convective ABLs via Eq. (1), two undesired effects indicate that pure GTMs are not suited for convective conditions:

- 1) the presence of heights with zero-mean tracer gradient and nonzero turbulent flux, implying  $K \rightarrow \infty$ ; and
- 2) the presence of heights where the turbulent flux and the mean gradient have the same sign, implying  $K < 0$ .

Both of these effects are unphysical considering the initial premise of GTMs that  $K(z)$  is akin to a diffusivity, and are linked to the presence of large convective plumes that can produce transport both with zero gradient and against the mean local gradient (countergradient transport) (Zhou et al. 2018). We refer to the appearance of these unphysical effects in pure GTMs applied to convective ABLs as GTM failure.

Wyngaard and Brost (1984, hereafter WB84) analyzed this issue and showed that GTM failure is a consequence of trying to parameterize the highly asymmetric vertical transport in convective ABLs using only one diffusive term. There are many examples of attempts to overcome this issue (Hamba 1993; Stull 1993; Fiedler 1984; Wyngaard and Weil 1991; van Dop and Verver 2001), but in this manuscript we focus on the approach usually attributed to Deardorff (1966, hereafter D66), which consists of adding an extra term  $F_{ND}$  to Eq. (1) which does not depend on local properties of the flow:

$$\langle w'c' \rangle = -\underbrace{K(z) \frac{\partial \langle C \rangle}{\partial z}}_{F_D(z)} + F_{ND}(z), \quad (2)$$

which is general enough to work in convective [where  $F_{ND}(z) \neq 0$ ] and neutral or stable conditions [where one would expect  $F_{ND}(z) \approx 0$ ]. In D66's original work  $F_{ND}$  is assumed to have the same shape as  $K(z)$  [see Eq. (9)], but we relax this assumption here. This model introduces a conceptual separation of the flux into two components: a diffusive component  $F_D = -K \partial \langle C \rangle / \partial z$ , which is conceptually tied to the small eddies of the flow, and a

<sup>a</sup> ORCID: 0000-0003-0854-3803.

<sup>b</sup> ORCID: 0000-0003-0576-0597.

Corresponding author: Marcelo Chamecki, chamecki@ucla.edu

nondiffusive component  $F_{\text{ND}}$ , which is conceptually tied to the action of large eddies (in this case, large convective plumes). This decomposition has been widely accepted by the community and it is used in many different forms, mostly distinct by their formulations for  $K$  and  $F_{\text{ND}}$  (D66; Holtslag and Moeng 1991; Siebesma et al. 2007; Ghannam et al. 2017). It should be noted that in most uses of D66's approach, the goal was parameterizing heat fluxes, but they are used here for examining passive tracers.

The main issue with Eq. (2) is that the addition of another unknown without an extra equation produces an underdetermined system and prevents us from directly estimating  $K(z)$  and  $F_{\text{ND}}(z)$  from measured quantities. Since there is no well-defined scale separation between “large” and “small” eddies in ABL flows, any diffusive/nondiffusive decomposition is bound to be artificial. Two workarounds are usually employed. One of them is to introduce an extra prognostic equation for the turbulent fluxes and, after several approximations, reach a separation of the fluxes into diffusive and nondiffusive components which can be used to infer  $K(z)$  and  $F_{\text{ND}}(z)$  [e.g., Holtslag and Moeng (1991) and Ghannam et al. (2017) for temperature]. The second workaround is to assume *a priori* shapes and/or scalings for both components (Troen and Mahrt 1986, hereafter TM86). We refrain from using both approaches here in order to avoid constraining our results.

To that end we introduce an optimization-based method that is capable of estimating profiles for  $F_D$  and  $F_{\text{ND}}$  without any imposed shape or scaling. Our focus lies on the diagnostic study of transport of passive tracers, although a brief analysis for temperature is included at the end. The case of momentum has extra complications (due to  $K(z)$  being a tensor) which are beyond the scope of the present work. Our method works in any ABL regime (stable, neutral, and unstable) and it only requires that two separate tracers with different sources into the interior be present. We apply our method to four large-eddy simulations (LESs) that range from weakly stable to strongly unstable and show that it captures general features that are expected from our understanding on ABL dynamics and modeling. Our results are then analyzed in reference to currently used models and used to discuss model development practices.

## 2. Theoretical aspects and definitions

Throughout this work, we use the word “separation” rather loosely to indicate a conceptual partition of the total turbulent flux into different terms, each tied to a different physical process, which can then be separately modeled. Conversely, we use the word “decomposition” in a mathematical sense, where an observed total flux is exactly decomposed into different terms that, by definition, exactly add up to the original flux.

A brief discussion on nomenclature practices is useful here. The first and second terms on the right-hand side of Eq. (2) are usually referred to as local and nonlocal terms. This is a reference to both the modeling of these terms (which depend on local and nonlocal flow quantities) and their intent to represent fluxes due to “local” and “nonlocal” processes (interpreted here as small eddies that remain localized in space and all remaining eddies, respectively; Moeng and Sullivan 1994). However, it is up for debate whether  $F_D$  and

$F_{\text{ND}}$  actually represent the turbulent vertical fluxes due to local and nonlocal processes (Zhou et al. 2018). Thus, this nomenclature is somewhat misleading since it blurs the line between the physical processes themselves and our attempt to parameterize them, while erroneously implying that a clear separation between both physical processes exist. Therefore, we use the names diffusive and non-diffusive fluxes for  $F_D$  and  $F_{\text{ND}}$ , which focuses on their mathematical form.

### a. Surface-forced and entrainment-forced transport

The concept of surface-forced versus entrainment-forced transport was first introduced by WB84, who noticed that tracer transport from the bottom up was more effective than from the top down in a convective ABL, with the source of asymmetry being the presence of organized coherent plumes emerging from the surface. Throughout our paper we refrain from using the terminology top-down and bottom-up (which is WB84's nomenclature) in favor of using the more general terms surface-forced and entrainment-forced tracers (SFT and EFT, respectively). We thus define an SFT as a tracer which has a source at the surface and no other sources/sinks in the domain. We denote its concentration with  $C_{\text{SFT}}$  and the subscript SFT is used throughout the paper to indicate quantities associated with this tracer. Figure 1a shows the normalized mean turbulent flux profile for an SFT in a convective regime as a solid black line (the simulation used for this plot will be detailed in section 3). SFTs are effectively transported in convective ABLs since their main transport mechanism is advection by coherent motions due to large convective plumes (Kaimal et al. 1976; Moeng and Sullivan 1994), which is sketched in Fig. 1a as red arrows.

An EFT, on the other hand, is defined as a tracer whose flux into the ABL is performed solely by entrainment processes; a mechanism that is sketched in Fig. 1b as blue arrows. In practice this flux occurs due to a change in concentration across the entrainment layer. Figure 1b also shows the mean turbulent flux profile for an EFT as a solid black line. Concentrations for EFTs are denoted as  $C_{\text{EFT}}$  and the subscript EFT is used throughout the manuscript to identify quantities associated with it. We use EFTs to define the maximum entrainment depth  $z_e$  and the top of the entrainment layer  $z_T$ :  $z_e$  is the height at which the turbulent flux of an EFT is at its minimum (as can be seen by the red dashed line in Fig. 1), and  $z_T$  is the height at which the mean turbulent flux of an EFT goes to roughly zero (excluding the surface) and can be seen in Fig. 1 as a dashed brown line.

It should also be noted that SFTs and EFTs span most passive tracers of interest. While passive tracers with surface sources are represented by SFTs and passive tracers with entrainment sources are represented by EFTs, passive tracers with sources in both boundaries are linear combinations of both. The exceptions that cannot be represented by these two cases are tracers with sources/sinks in the interior of the ABL.

### b. Flux decompositions and models

Equations (1) and (2) are two different flux separations on which most models are based. We proceed with a brief

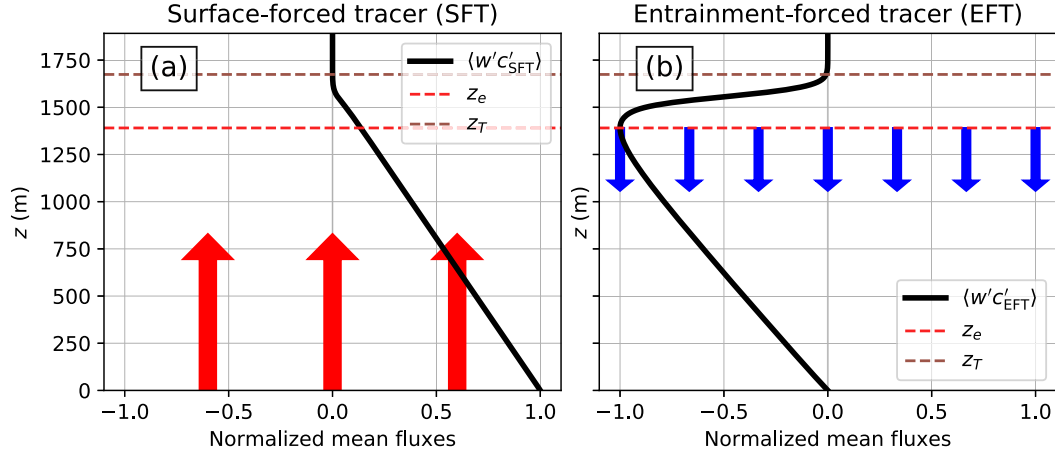


FIG. 1. Mean turbulent flux profiles for (a) an SFT and (b) an EFT. The data for this plot are taken from simulation Plumes, to be described in section 3. Both fluxes are normalized so that the maximum magnitude of the fluxes is unity. Also sketched in the figure are arrows for transport via coherent convective plumes (red arrows) and entrainment processes (blue arrows), and the maximum-entrainment height  $z_e$  and entrainment-layer top  $z_T$  (dashed lines; see key).

description of some models of interest to this research and their approaches to partitioning fluxes. The reader is directed to van Dop and Verver (2001) and Ghannam et al. (2017) for more information on the models.

#### 1) FULLY DIFFUSIVE

Fully diffusive separations are pure GTMs and follow Eq. (1). In the case of fully diffusive decompositions, the total turbulent flux is treated as one diffusive process only and the result is trivial:  $F_{ND} = 0$  and  $F_D = \langle w'c' \rangle$ .

An early example of a fully diffusive model is given by Prandtl (1942), who estimated the eddy diffusivity with a mixing length approach. Another example is the one by WB84, where the asymmetry of the flow (transport from the top-down vs bottom-up) is understood as two separate diffusive processes that act alongside each other. Thus in WB84's model the total eddy diffusivity  $K(z)$  depends on the bottom-up diffusivity  $K_{SFT}$ , associated with convective plumes, and on the top-down diffusivity  $K_{EFT}$ , associated entrainment processes. Since transport via convective plumes is more efficient than via small eddies,  $K_{SFT} > K_{EFT}$  for most of any convective ABL. Their method can be written as

$$K_{SFT}(z) = -\frac{\langle w'c'_{SFT} \rangle}{\partial \langle C_{SFT} \rangle / \partial z}, \quad (3)$$

$$K_{EFT}(z) = -\frac{\langle w'c'_{EFT} \rangle}{\partial \langle C_{EFT} \rangle / \partial z}, \quad (4)$$

$$K_i(z) = \frac{K_{SFT}K_{EFT}[\langle w'c'_i \rangle_s(1 - z/z_e) + \langle w'c'_i \rangle_e z/z_e]}{K_{EFT}\langle w'c'_i \rangle_s(1 - z/z_e) + K_{SFT}\langle w'c'_i \rangle_e z/z_e}, \quad (5)$$

where  $\langle w'c'_i \rangle_s$  and  $\langle w'c'_i \rangle_e$  are the tracer's turbulent flux at the surface and at the entrainment layer, respectively, and the subscript  $i$  differentiates between tracers. Although conceptually useful, WB84's model is of limited practical applicability due to GTM failure and because  $K_i(z)$  depends on the ratio

$\langle w'c'_i \rangle_e / \langle w'c'_i \rangle_s$  for specific tracers (thus it is no longer a property of the flow alone).

#### 2) ONE DIFFUSIVE AND ONE NONDIFFUSIVE COMPONENT

This case follows Eq. (2) and  $F_{ND}$  is a single term that can be estimated in various ways (Holtslag and Moeng 1991; Ghannam et al. 2017), resulting in a two-term flux partition. TM86 popularized it with their model, which can be written as

$$K(z) = u_s(z)hG(z/h), \quad (6)$$

$$u_s(z) = \frac{\kappa u_*}{\phi(z/L_o)}, \quad (7)$$

$$G(z/h) = \frac{z}{h} \left(1 - \frac{z}{h}\right)^2, \quad (8)$$

$$F_{ND} = C_* G(z/h) \langle w'c' \rangle_s, \quad (9)$$

where  $\kappa = 0.4$  is the von Kármán constant,  $C_*$  is a constant,  $\phi$  is the nondimensional gradient for a tracer in the surface layer,  $G$  is a cubic shape function,  $h$  is the ABL height, and the velocity scale  $u_s$  is capped at its value at  $z/h = 0.1$  for unstable conditions.

One other approach to model  $F_{ND}$  is the eddy-diffusivity mass-flux (EDMF) method, whose premise is to explicitly separate the flux due to narrow convective plumes and the rest of the flow (generally referred to as the environment). The governing equations for this method follow naturally from the updraft-environment separation and, after assuming that updrafts are arbitrarily narrow (Siebesma et al. 2007), the non-diffusive flux becomes

$$F_{ND} = M(\langle C \rangle_u - \langle C \rangle), \quad (10)$$

where  $M$  is the vertical mass flux and  $\langle C \rangle_u$  is the average concentration of a tracer inside updrafts. To model the total

turbulent flux,  $F_{ND}$  is then combined with a parameterization for  $K(z)$  similar to Eq. (6). It is worth noting that this approach is designed to work well in strongly convective conditions (Siebesma et al. 2007; Witek et al. 2011).

Although estimating the terms of a fully diffusive decomposition is trivial, doing the same for a two-term decomposition is challenging due to the resulting underdetermined system of equations. One example that relies on fitting eddy diffusivities in a plume of passive scalars has been used in the oceanic sciences community (Chen et al. 2016) and a different approach is introduced in the present work. It is worth noting that approaches to decompose the total flux exist, but all of them focus on separating it into components due to local and nonlocal processes without assuming a diffusive/nondiffusive separation. These approaches are built with convective conditions in mind and rely on some type of conditional sampling of the instantaneous velocity fields (see Zhou et al. 2018, and references therein, and Chinita et al. 2018).

### c. Criteria for separation

In this section we discuss a set of criteria that are in accordance with what is currently known about the dynamics and modeling of ABLs. These criteria are desired of both decompositions and models based on them, and should be observed by both SFTs and EFTs. It is important to emphasize that there exist many decompositions that satisfy these criteria, and these are merely reality checks that are necessary but not sufficient for a decomposition to be considered successful. With that in mind, we proceed to list the criteria and discuss them:

- 1)  $K(z)$  should be only a property of the flow and independent of the tracer;
- 2)  $K(z)$  should be a finite nonnegative quantity everywhere;
- 3)  $K(z)$  should follow Monin–Obukhov similarity theory (hereafter MO similarity theory) within the surface layer for tracers whose main flux into the ABL happens through the surface.

Although criterion 1 may appear to always be true for passive tracers, this can only be theoretically justified under specific conditions. Let us define a length scale  $l^c$  as the distance over which the mean gradient  $\partial\langle C \rangle / \partial z$  remains relatively constant (Corrsin 1975). Note that  $l^c$  may be different for different tracers. Let us also loosely define the integral scale of the flow ( $l^I$ ) as the size of the largest eddies. Since only the effect of eddies smaller than  $l^c$  can be theoretically included in  $K(z)$ , then criterion 1 should only be true when  $l^I < l^c$  (Corrsin 1975) and a tracer-independent  $K(z)$  should be viewed as an approximation for all other cases. In practice, however, this approximation seems to be valid since tracer-independent eddy diffusivities have been used for decades (although often there is the introduction of Prandtl and Schmidt numbers; Elliott and Venayagamoorthy 2011; Li 2019) and have been shown to produce reasonable results. We thus include criterion 1 mostly based on modeling purposes.

Criterion 2 prevents GTM failure and ensures that there is integrated variance reduction for any transported scalar. Criterion 3 is based on empirical observations that, when the necessary assumptions are satisfied, MO similarity theory

appears to hold well. This condition is built into all eddy-diffusivity parameterizations that assume an a priori shape for  $K$  (e.g., TM86; Holtslag and Moeng 1991), but may not be true if  $K$  is calculated based on a decomposition.

It is important to note that that criterion 1 is formulated with passive tracers in mind and should not be expected to hold exactly for active tracers, which are cases that could have different values of eddy diffusivities. Criteria 2 and 3, however, are expected to also hold for temperature and momentum. Although these criteria are known to be satisfied in neutral ABLs, all of them are expected to hold for passive tracers independently of stability.

Considering the decompositions used by the models previously described here (using one and two components), it is straightforward to verify that they do not satisfy all three criteria. We illustrate this fact for selected cases in the appendix.

Note that Siebesma et al. (2007) introduce similar criteria which include the constraint that  $\text{MAX}(K)/(w_* z_e) \approx 0.1$ . However, this is not strictly required by any physical arguments and the reason why virtually all parameterizations since TM86 exhibit this feature is that a cubic shape function is the lowest degree polynomial that can satisfy all physically motivated boundary conditions for  $K(z)$  (O'Brien 1970), which happens to have a maximum of  $\approx 0.15$  at  $1/3$  of the domain.

### d. Satisfying the criteria and decomposition options

All of the flux separations reviewed so far divide the total flux into either one or two components. Since decompositions based on these separations fail at least one of the consistency criteria, we argue for a broader three-term decomposition. Thus, instead of one nondiffusive component, we argue for two nondiffusive components in addition to the diffusive term:

$$\langle w'c' \rangle = -K(z) \frac{\partial \langle C \rangle}{\partial z} + \underbrace{\Gamma_s(z) + \Gamma_e(z)}_{F_{ND}}, \quad (11)$$

where  $\Gamma_s$  and  $\Gamma_e$  are separate nondiffusive fluxes more clearly defined below. The main motivator for a decomposition into three terms is that it makes it possible for all three of the aforementioned criteria to be satisfied simultaneously.

Since most tracers in the atmosphere exchange mass with the ABL via surface and/or entrainment processes (idealized here as SFTs and ETFs, respectively), we can conceptually link  $\Gamma_s$  to surface fluxes (and thus convective plumes) and  $\Gamma_e$  to fluxes at the entrainment. This allows one to rewrite Eq. (11) as

$$\langle w'c' \rangle = -K(z) \frac{\partial \langle C \rangle}{\partial z} + \langle w'c' \rangle_s G_s + \langle w'c' \rangle_e G_e, \quad (12)$$

where  $\Gamma_s = \langle w'c' \rangle_s G_s$  and similarly for  $\Gamma_e$ . Here,  $\langle w'c' \rangle_s$  and  $\langle w'c' \rangle_e$  are the values of the turbulent flux  $\langle w'c' \rangle$  taken at the surface and at  $z = z_e$ , respectively. Furthermore,  $G_s$  and  $G_e$  are dimensionless shape functions (with their height dependence omitted for brevity) which are assumed to be a function of the flow alone. Thus, knowledge of  $K$ ,  $G_s$ , and  $G_e$  is sufficient to reconstruct the total flux of any tracer provided that the fluxes at the vertical boundaries of the ABL are known. Given our focus on diagnostic analyses, we obtain  $\langle w'c' \rangle_s$  and  $\langle w'c' \rangle_e$  from

LES results. However, assuming knowledge of these quantities (especially  $\langle w'c' \rangle_e$ ) may be problematic if Eq. (12) is used to develop prognostic models, in which case they may need to be parameterized.

Although our experience with entrainment fluxes suggests that  $G_e(z)$  is small, our criteria suggests that it may be necessary in some conditions. We thus consider the general three-term decomposition in Eq. (12) throughout our manuscript and rely on results from numerical simulations to indicate the relative importance of  $G_e(z)$  (see section 5).

#### e. Estimating the components

To decompose the flux using three terms according to Eq. (12) we need  $K(z)$ ,  $G_s$  and  $G_e$ . We estimate these functions assuming no a priori scaling or shape for either of them by considering an SFT and an EFT subjected to the same flow (and thus with the same  $K(z)$ ,  $G_e$ , and  $G_s$ ), which leads to the following system of equations:

$$\langle w'c'_{\text{SFT}} \rangle = -K(z) \frac{\partial \langle C_{\text{SFT}} \rangle}{\partial z} + \langle w'c'_{\text{SFT}} \rangle_e G_e + \langle w'c'_{\text{SFT}} \rangle_s G_s, \quad (13)$$

$$\langle w'c'_{\text{EFT}} \rangle = -K(z) \frac{\partial \langle C_{\text{EFT}} \rangle}{\partial z} + \langle w'c'_{\text{EFT}} \rangle_e G_e. \quad (14)$$

Note that while an SFT has both components of the non-diffusive flux (since there may be a small flux of  $C_{\text{SFT}}$  through  $z_e$ ), an EFT only has the entrainment-driven flux, since  $\langle w'c'_{\text{EFT}} \rangle_s = 0$  as a boundary condition.

Exact closures are possible by making extra assumptions (such as  $G_e = 0$ ), but as was mentioned before, these options all fail one or more of the introduced criteria (see the appendix). The approach proposed here is to introduce an optimization method that uses only fluxes and mean scalar gradients of SFTs and EFTs in order to estimate an eddy diffusivity profile. To that end, we introduce a cost function  $\chi$  to be minimized in an optimization procedure, which can be written generally as

$$\chi = \mathcal{F}(K, G_s, G_e). \quad (15)$$

Although the definition of  $\chi$  is ultimately arbitrary, we choose it so that nondiffusive fluxes  $F_{\text{ND}}$  are minimized, while still accommodating the fact that  $K(z)$  is equal for every scalar being transported. This choice is mainly motivated by modeling purposes, but partially by physical arguments. Most of the modeling motivation comes from decades of experience with diffusive closures, which have shown that  $F_D$  alone can be very powerful in modeling fluxes (Corrsin 1975). Furthermore, diffusive operators are numerically well behaved, easy to implement, and ubiquitous throughout the atmospheric community. Finally, as a physical motivation, we know that in some regimes (such as neutral or stable) the coherent structures are generally small (Jayaraman and Brasseur 2018) and the flux is mostly diffusive (see section 4), and by minimizing  $F_{\text{ND}}$  we ensure that such situations are captured by our approach. The chosen cost function for this purpose can be written as

$$\chi = G_s^2 + G_e^2. \quad (16)$$

It should be noted that there are different ways to formulate a cost function that minimizes  $F_{\text{ND}}$  (e.g., using absolute value operators or using fourth powers instead of second powers). We have tried several other variations and found that, while the results are qualitatively similar to results using Eq. (16), some of the features were less appealing from a physical perspective.

The optimization can be made in two ways and both will be analyzed here. In both cases the constraint that  $K \geq 0$  is enforced but in the simplest approach  $G_e$  and  $G_s$  are left unconstrained and can become negative at some regions of the ABL. This option is called the unconstrained version of the optimization. The alternative (constrained version) is to impose that both  $G_e$  and  $G_s$  be always nonnegative, which avoids non-diffusive countergradient fluxes for SFTs and EFTs. Note that countergradient fluxes can happen in ABLs and so, a priori, both versions of the optimization are equally plausible.

We emphasize here that even though we make  $\chi$  a partly physically motivated function, its choice is ultimately arbitrary given the lack of a proper definition of diffusive and non-diffusive fluxes. We nonetheless show that our choice of  $\chi$  produces results that make physical sense as the final product (see section 4) and are easily reproducible in any simulation that contains an SFT and an EFT. Furthermore, although all results presented in this paper use an SFT and an EFT [see Eqs. (13), (14)], results using temperature and an EFT as the two scalars are very similar. This builds confidence in our method since temperature is very different from an SFT: not only is it an active tracer but it also has a significant entrainment-forced component. Using temperature and an SFT, however, produces poorer results, most likely because both scalars have very similar turbulent fluxes and gradients in the bottom half of the ABL, producing a system of equations that is approximately linearly dependent. Refer to section 5c for the extension of this method to temperature.

### 3. Numerical aspects

We use an LES model to apply the theory and methods introduced in section 2. Our model has been extensively validated and was already used in several other investigations (Kumar et al. 2006; Salesky et al. 2017). As a brief description, our model employs a pseudospectral scheme in the horizontal directions (with doubly periodic horizontal boundary conditions) and a centered finite difference in the vertical direction to solve the flow. The top one-quarter of the domain has a sponge layer to mimic an open boundary and we use a Lagrangian-averaged scale-dependent dynamic subgrid-scale model for closure (Bou-Zeid et al. 2005). The tracer advection is solved using a finite volume scheme embedded into the spectral code with bounded advection (Chamecki et al. 2008).

Four simulations are used in total and their main difference is the buoyancy forcing at the surface, which reflects four different stability conditions ranging from weakly stable to strongly unstable. The rotation frequency was set to  $1 \times 10^{-4} \text{ s}^{-1}$  in all cases and the grid has 256 points in the horizontal direction and 400 points in the vertical direction. Note that our model has been shown to converge at coarser resolutions than similar models with different subgrid-scale closures



TABLE 1. Parameters for the simulations used in this paper. All simulations have 256 points in the horizontal direction and 400 points in the vertical direction. Note that we show the negative real root corresponding to  $w_*$  for the stable case for the sake of simplicity.

Simulation	$\langle w'\theta' \rangle_s$ (m K s <sup>-1</sup> )	$u_*$ (m s <sup>-1</sup> )	$w_*$ (m s <sup>-1</sup> )	$L_o$ (m)	$L_x, L_y$ (m)	$L_z$ (m)	$z_e$ (m)	$z_T$ (m)
Stable	$-0.20 \times 10^{-2}$	0.15	-0.17	133.7	500	300	72.8	152.3
Neutral	0	0.20	0	$-\infty$	3000	1000	355.0	542.5
Rolls	$0.15 \times 10^{-2}$	0.23	0.29	-585.5	3500	1200	462.0	627.0
Plumes	$3.76 \times 10^{-2}$	0.28	1.22	-41.7	7680	2700	1390.5	1647.0

(Salesky et al. 2017). The initial potential temperature ( $\theta$ ) profile is well mixed until approximately 90% the reported ABL height with a constant gradient of  $2 \times 10^{-2}$  K m<sup>-1</sup> above it. Each simulation has a different domain length which can be found in Table 1 along with other parameters. Note that the names of the simulations reflect a regime characteristic. Simulations Stable and Neutral are named after their stability condition. Simulations Rolls and Plumes are both convective and are named after the main coherent structure that transports the quantities from the surface (Salesky et al. 2017). They can be both classified as weakly and strongly unstable, respectively (Jayaraman and Brasseur 2018). Note that Salesky et al. (2017) calls the strongly convective regime the “cell” regime, due to the horizontal imprint of convective plumes, but the dominating coherent structures are the plumes, which is why the present name was chosen.

The roughness length is set to  $z_0 = 1 \times 10^{-2}$  m throughout, and all simulations are forced with a geostrophic velocity of  $5 \text{ m s}^{-1}$  in the  $x$  direction imposed by a pressure gradient. We minimized the effects of inertial oscillations by setting the initial conditions for velocity to their average over one inertial period (taken from identical simulations that were run only for this purpose). All of the simulations had a spinup period of at least eight convective cycles  $T_*$  and the statistics were collected during the next  $8T_*$  period (calculated as  $T_* = z_e/\text{MAX}(u_*, w_*)$ , where the turbulent convective velocity is calculated as  $w_*^3 = g\langle w'\theta' \rangle_s z_e / \theta_s$  and  $\theta_s = 300$  K is a potential temperature scale).

All simulations also have two passive tracers: an SFT and an EFT with concentrations  $C_{\text{SFT}}$  and  $C_{\text{EFT}}$ , which have different initial and boundary conditions. Entrainment fluxes are accomplished, as previously discussed, by imposing different initial concentrations for the mixed layer and above it. Thus, EFTs are initialized with zero concentration until approximately  $0.9z_e$  and nonzero concentration above. SFTs are initialized with a  $C_{\text{SFT}} = 0$  throughout the domain. EFTs have a zero-flux boundary condition at the surface, while we impose a nonzero surface mass flux into the ABL for SFTs. Both tracers have horizontally periodic boundary conditions and a sponge layer assures that the top of the domain does not affect results in the ABL. Throughout this paper tracer fluxes are normalized either by their value at the surface or at  $z_e$ , so they are dimensionless. It is worth noting that for both tracers there is no steady state for the concentrations in the ABL (since there are sources but no sinks). However, our chosen averaging period ( $8T_*$ ) ensures that effects of time dependency are negligible.

We apply both versions of the optimization procedure introduced in section 2 (constraining  $G_s$  and  $G_e$  to be nonnegative

and not constraining them) using an optimization library freely available in the Python package SciPy (Virtanen et al. 2019). The optimization takes an initial guess for  $K(z)$ ,  $G_s$  and  $G_e$ , and iterates until an optimal solution is reached. Although the optimization approach proved to be mostly independent of the initial guess, we formalize it by always starting at the uppermost grid point (thus well into the stratified layer above the ABL) and setting the initial guess so that both  $K = G_s = G_e = 0$  (which is always approximately true in the stratified layer). We then proceed downward by using the result from the previous grid point as an initial condition for the next one.

#### 4. Results and discussion

In this section we present the results for  $F_D$  and  $F_{\text{ND}}$  based on our decomposition, and then move on to discuss the eddy diffusivity and shape function profiles. For visualization purposes, we normalize the vertical axis in all simulations by  $z_T$ . Note that it is useful to analyze results as a function of the bulk ABL stability  $-z_e/L_o$  which is equivalent to  $\kappa w_*^3/u_*^3$ .

##### a. Diffusive–nondiffusive flux decompositions

Figures 2 and 3 show results for simulations Stable and Neutral, respectively. In both regimes results for the unconstrained (top rows) and constrained (bottom rows) optimizations

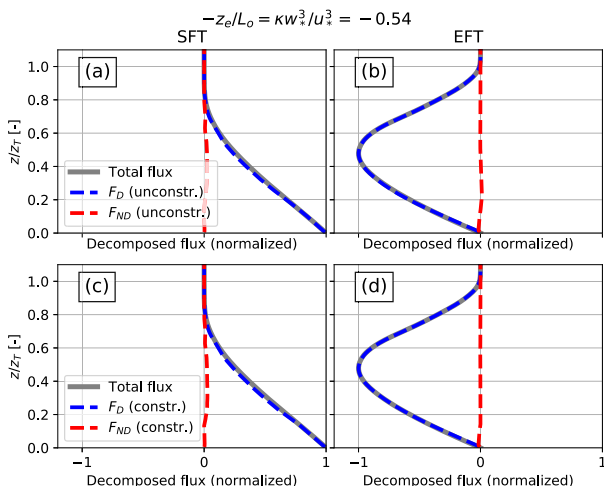


FIG. 2. Decomposition of mean turbulent tracer fluxes of simulation Stable for the (a),(b) unconstrained optimization approach and (c),(d) constrained approach. Results are shown for (a),(c) the SFT and (b),(d) the ETF. Black lines are the total flux, blue lines show the diffusive component, and red lines show the nondiffusive component.

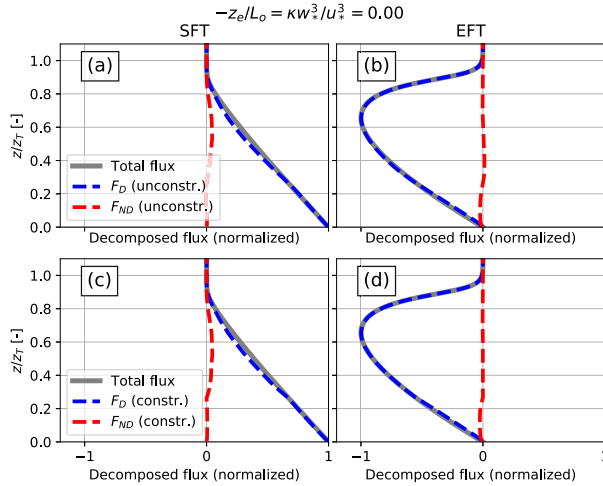


FIG. 3. Decomposition of mean turbulent tracer fluxes of simulation Neutral for the (a),(b) unconstrained optimization approach and (c),(d) constrained approach. Results are shown for (a),(c) the SFT and (b),(d) the EFT. Black lines are the total flux, blue lines show the diffusive component, and red lines show the nondiffusive component.

are very similar and the diffusive components dominate the flux in all cases. This result is in agreement with our expectations for neutral and stable conditions, where the total turbulent fluxes are mostly accomplished by small eddies and are likely to be well represented by  $F_D$  alone.

Figure 4 shows results for simulation Rolls, where we see that, in general, nondiffusive fluxes are not negligible. The nondiffusive contribution is especially important for the SFT, as one would expect, indicating the role of large coherent flow structures in transporting the mass when the tracer source is located at the surface even in weakly convective regimes. Although there are some differences between the constrained and unconstrained optimizations, they are qualitatively very similar.

Figure 5 shows results for simulation Plumes, where we see that a significant portion of the fluxes is performed by the nondiffusive component, as is expected from our knowledge of convective ABLs. For both the constrained and unconstrained optimizations, the majority of the fluxes for the SFT are nondiffusive. Once again, although the constraints do modify the results, there is no qualitative difference between both approaches for the SFT. For the EFT, both optimizations show a smaller importance of nondiffusive fluxes compared to the SFT. However, while the unconstrained version shows a nonnegligible countergradient flux for the EFT around  $z/z_T = 0.2$ , the constrained optimization produces almost no nondiffusive fluxes in this case. It is worth mentioning that the resulting diffusive–nondiffusive decompositions for an SFT in this regime are very similar to results for temperature shown in Fig. 7d of Siebesma et al. (2007).

Thus, for most decompositions in the regimes analyzed here the choice of a constrained versus an unconstrained optimization does not qualitatively change the results. The exception is the EFT in simulation Plumes, which exhibits regions of

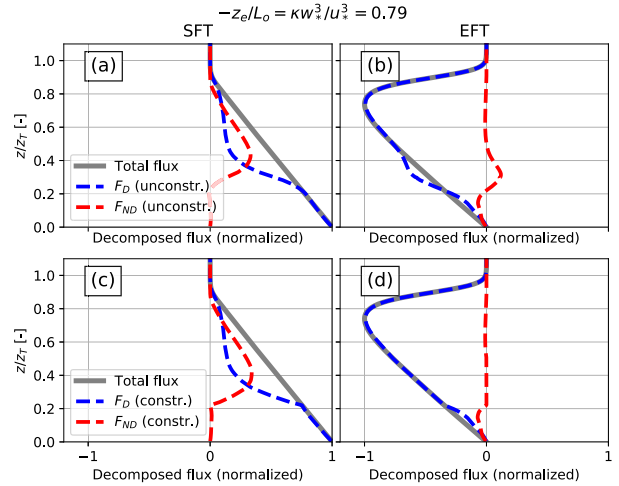


FIG. 4. Decomposition of mean turbulent tracer fluxes of simulation Rolls for the (a),(b) unconstrained optimization approach and (c),(d) constrained approach. Results are shown for (a),(c) the SFT and (b),(d) the EFT. Black lines are the total flux, blue lines show the diffusive component, and red lines show the nondiffusive component.

negative values for  $G_e$  in the unconstrained optimization, implying countergradient nondiffusive fluxes due to entrainment. Although this feature does not immediately fit into our current understanding of transport in convective ABLs, it is not an impossibility (given that not much has been explored about the specific dynamics of tracer transport from the stratified free troposphere into the ABL) and there are no grounds to consider one optimization approach superior to the other with the present data.

Furthermore, in the separation between local and nonlocal fluxes proposed by Zhou et al. (2018), there is evidence that much of the entrainment flux in convective regimes is accomplished by nonlocal fluxes. Our results indicate that despite that fact this flux can be successfully parameterized as a diffusive process.

#### b. Eddy diffusivities and shape functions

We dedicate this section to the analysis of  $K(z)$ ,  $G_s$ , and  $G_e$  obtained through our optimization. We use TM86's model, given in Eqs. (6)–(9), as a qualitative reference when discussing results. For optimal results  $h$  is chosen on a case-by-case scenario to approximately match the height at which the estimated eddy diffusivities go to zero (which is the effect it has on  $G(z/h)$ ). This is done in order for us to focus on the comparison of the eddy diffusivities without worrying about the precise estimation of  $h$ . We use the empirical similarity functions  $\phi$  given in Large et al. (1994) for all regimes, which is based on data for the atmosphere and follows the 1/3 scaling in the convective limit (Kader and Yaglom 1990; Katul et al. 2011). In our implementation we set  $C_* = 6.5\kappa$  in all cases to match TM86's choice.

Since the neutral case is the most well-studied ABL regime, we start with Fig. 6, which shows different estimations of  $K(z)$  for simulation Neutral. The ABL height in TM86's profile is set

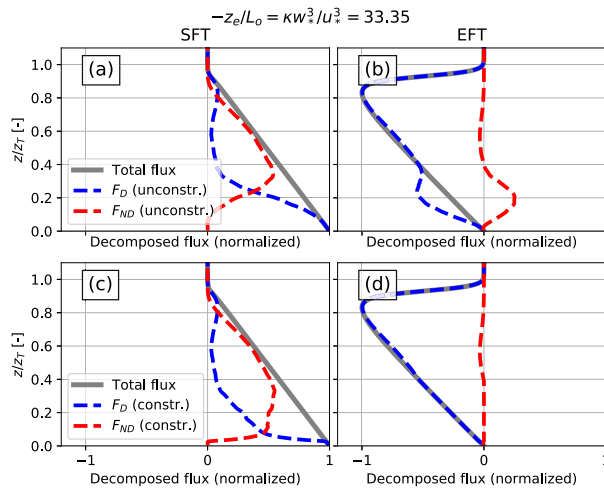


FIG. 5. Decomposition of mean turbulent tracer fluxes of simulation Plumes for the (a),(b) unconstrained optimization approach and (c),(d) constrained approach. Results are shown for (a),(c) the SFT and (b),(d) the ETF. Black lines are the total flux, blue lines show the diffusive component, and red lines show the nondiffusive component.

to  $h = 0.9z_T$ . Figure 6a shows results for the entire ABL, where we can see that all estimates are very similar, which is expected. The surface-forced eddy diffusivity  $K_{SFT}$  is shown only for reference and is the result of assuming  $F_{ND} = 0$ ; thus it is not a part of our method. Note also that  $K_{EFT}(z)$ , which is also not part of our method, is very similar to the other curves shown (as expected) but it is not depicted for brevity. Figure 6b zooms in on the lower ABL, where we can see that all estimates of  $K(z)$  approximately match MO similarity theory in the surface layer (given by TM86's profile, which is built to follow MO similarity theory close to the surface). We attribute the small deviation to inherent limitations of the subgrid-scale models and wall models employed as part of the LES technique (Khanna and Brasseur 1997; Porté-Agel et al. 2000; Bou-Zeid et al. 2005; Brasseur and Wei 2010) and consider that  $K(z)$  satisfies criterion 3.

Figure 7 shows eddy diffusivity estimations for simulations named Stable, Rolls, and Plumes. The ABL heights for TM86's model is  $h = 0.95z_T$  for Stable and  $h = 0.9z_T$  for Rolls and Plumes. Note that for the stable case (Fig. 7a) all curves are similar to each other, including the reference TM86 profile, which is not true for the other cases, where there is a clear difference between the cubic profiles from TM86 and our estimations from the optimization procedure.

For the weakly convective case (Fig. 7b) there is a small difference between the constrained and unconstrained approaches, but both produce significantly larger values than TM86's profile. Although there is some ambiguity when defining  $h$ , it cannot account for a discrepancy that large. The  $K(z)$  estimations for the strongly convective case (Fig. 7c) are also distinct, with clear differences in shape and magnitude between them.

In all cases (including simulation Neutral) the eddy diffusivity profiles are mostly of convex shape, with an approximately zero derivative at  $z_e$ . Furthermore, the peak value seems to always be located in the lower portion of the ABL.

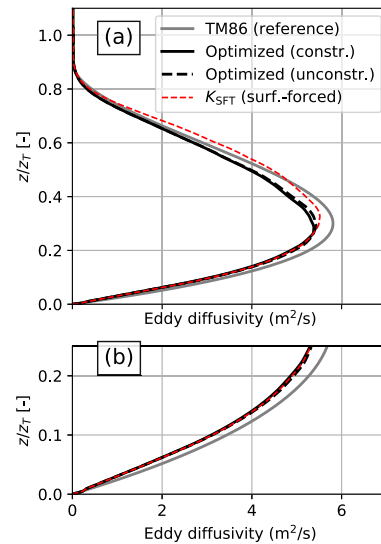


FIG. 6. (a) Estimation of the eddy diffusivity for simulation Neutral using the constrained optimization (solid black lines) and the unconstrained optimization (dashed black lines). Also shown for reference are the SFT's eddy diffusivity  $K_{SFT}(z)$  [dashed red line; obtained via Eq. (3)] and TM86's parameterization (solid gray line). (b) As in (a), but zoomed in on a lower range of the vertical axis.

We emphasize that these features (which are imposed in most eddy diffusivity parameterizations) are not imposed in any way in our optimization procedure, but emerge naturally.

Our optimization-based estimates for simulations Rolls and Plumes are replotted in Fig. 8 along with  $K_{SFT}(z)$  and  $K_{EFT}(z)$ . Note that in both panels  $K_{SFT}$  is significantly larger than  $K_{EFT}$ . This is expected and it occurs because SFTs are transported vertically by strong coherent updrafts, making them much more well mixed (and with a much lower vertical gradient) than EFTs for a similar turbulent flux, thus producing a larger eddy diffusivity through Eqs. (3) and (4) (WB84).

In Fig. 8, both optimized  $K(z)$  follow  $K_{SFT}(z)$  at the bottom of the domain (thus obeying criterion 3) and  $K_{EFT}(z)$  at the top of the domain. (Note that for the Plumes case the constrained  $K(z)$  follows  $K_{SFT}$  only in a small percentage of the surface layer.) It is likely that  $K_{SFT}$  and  $K_{EFT}$  are more relevant in these respective regions, which builds confidence in our optimization. Note also that while the  $K(z)$  from our unconstrained optimization lies in between both  $K_{SFT}$  and  $K_{EFT}$  in a significant region in the middle of the ABL, the constrained version appears to simply switch between both, being approximately equal to  $K_{SFT}$  in the lower ABL and  $K_{EFT}$  in the upper ABL. This opens the possibility of approximating the resulting  $K(z)$  for the constrained optimization as  $K(z) = \text{MIN}(K_{SFT}, K_{EFT})$ , which is a much faster calculation. Finally,  $K_{EFT}$  alone appears to be a somewhat good approximation of  $K(z)$  calculated with the unconstrained optimization (with the caveat that  $K_{EFT}$  does not follow the MO similarity theory prediction at the surface).

Figure 9 shows the shape functions  $G_s$  (left) and  $G_e$  (right) and each row corresponds to a different case, indicated on the



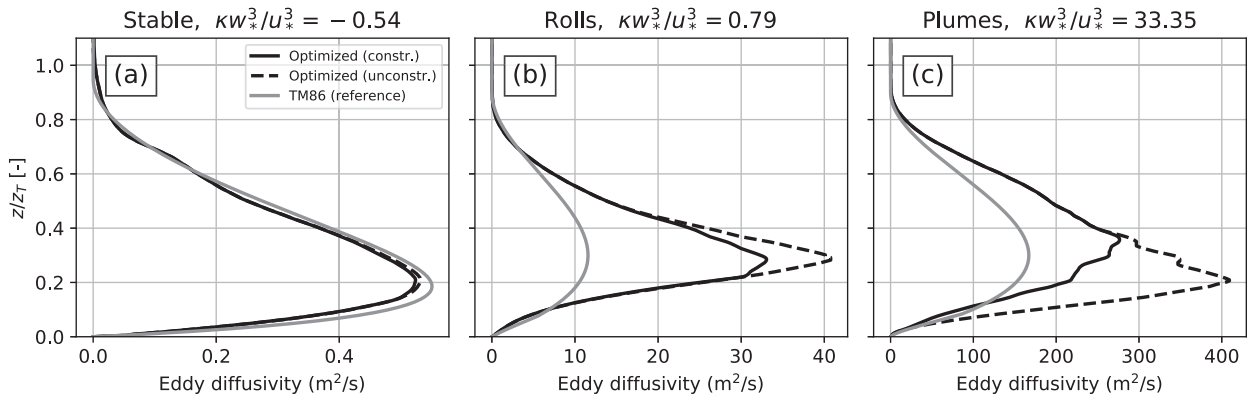


FIG. 7. Estimates for eddy diffusivity  $K(z)$  for nonneutral simulations (a) Stable, (b) Rolls, and (c) Plumes. Solid black lines are results for the constrained optimizations, dashed back lines are results for the unconstrained optimization, and solid gray lines are results TM86 for reference.

right side of the figure. Note that the shape functions for simulations Stable and Neutral have small values in all cases, as can be anticipated by the results from Figs. 2 and 3. This is not the case for unstable conditions, where we see magnitudes close to 0.4 and 0.6 for  $G_s$ . Although it is tempting to interpret this fact as indicating that up to 60% of the tracer flux at surface is carried via nondiffusive processes, this is not strictly true since the total flux changes with height.

There is no significant qualitative difference between the constrained and unconstrained optimizations for  $G_s$  in the unstable cases (Figs. 9e,g). Furthermore,  $G_s$  shapes are similar between these two simulations (with the possible exception of the magnitudes near the surface). Together with the fact that the nondiffusive fluxes appear to be approximately zero in stable and neutral regimes, this makes it relatively easy for an analytical model to capture this behavior with a convex function for  $G_s$ .

The shape function  $G_e$ , however, exhibits significant difference between both optimization approaches in the unstable regimes (Figs. 9f,h). The unconstrained optimization results in significant negative values for  $G_e$  in the unstable simulations (especially for simulation Plumes), indicating countergradient fluxes performed by entrainment processes. The constraints for  $G_e$  avoid this behavior, resulting in a much smaller contribution of nondiffusive entrainment processes. This poses a challenge for modeling such components and indicates that using the constrained version of the optimization produces results that may be advantageous for modeling purposes. This issue will be further explored in section 5. It should be noted that it is counterintuitive that  $G_e$ , an entrainment-driven nondiffusive transport, makes corrections in the lower ABL, as opposed to the upper ABL.

It should also be noted that we expect  $G_s \approx 0$  from the surface until  $\approx \text{MIN}(0.1z_e, -L_o)$  according to MO similarity theory, indicating that SFT fluxes are fully diffusive in that region (Kaimal and Finnigan 1994, section 1.4.2). While all of the shapes respect that,  $G_s$  for simulation Plumes (Fig. 9g) is in approximate violation for the constrained optimization. Although it should also be noted that the upper limit for this range (in the Plumes case  $L_o/z_T \approx 0.03$ ) comes from scale

analysis and is therefore approximate. While some features of the constrained optimization allow for simplifications when modeling (see section 5), this feature in particular is undesirable from a physical point of view. Note also that  $G_e$  does not need to respect this rule since it is associated with entrainment fluxes, rather than surface fluxes, and need not be subject to MO similarity theory restrictions.

Finally, we note that there are clear differences in the decomposition between the simulation in the rolls and plumes regimes. This is in contrast to the results of the local/nonlocal decomposition of Zhou et al. (2018), where the decompositions for both regimes are very similar (see their Fig. 5).

## 5. Overall tendencies and implications for modeling

Although three terms are necessary for all three plausibility criteria to be satisfied in decompositions, parameterizations are always approximations and can satisfy all criteria with only two terms. With that in mind, we proceed to analyze the results from the previous section in terms of bulk quantities and discuss them in the context of model development.

Note that since we only have four data points (one for each simulation) any interpolation to intermediate

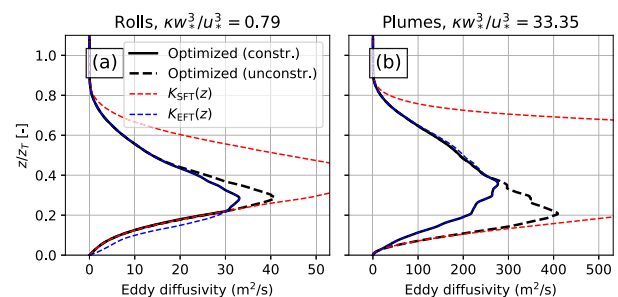


FIG. 8. Estimates for eddy diffusivity  $K(z)$  for nonneutral simulations (a) Rolls and (b) Plumes. Solid black lines are results for the constrained optimizations, dashed back lines are results for the unconstrained optimization, dashed red lines are results TM86 for the surface-forced eddy diffusivity  $K_{\text{SFT}}$ , and dashed blue lines are results for the entrainment-forced eddy diffusivity  $K_{\text{EFT}}$ .

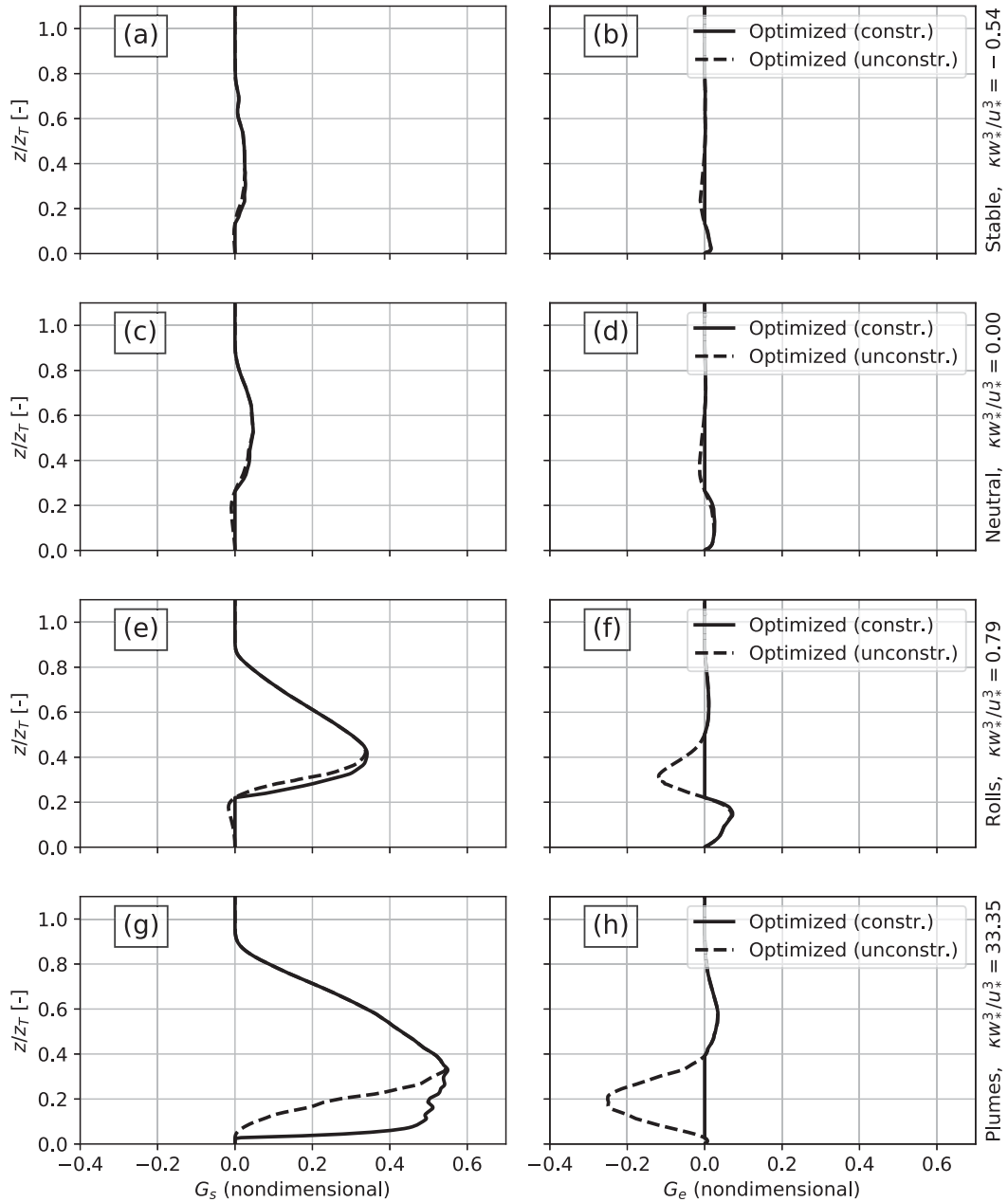


FIG. 9. Shape functions (left)  $G_s$  and (right)  $G_e$ . Different rows show results for different simulations, whose names are indicated on the right side of the figure. Solid black lines are results for the constrained optimizations and dashed back lines are results for the unconstrained optimization.

stability conditions other than the ones presented should be done with care. For this reason, we make no attempt at creating a novel model based on our results, which would require a larger set of stability regimes to be investigated.

#### a. Bulk analysis of flux partition

We gain context by quantifying the importance of nondiffusive fluxes in different stability regimes. For that purpose, we define a bulk measure  $R_F$  as

$$R_F = \left[ \frac{\int_0^\infty F_{ND}^2 dz}{\int_0^\infty (F_D^2 + F_{ND}^2) dz} \right]^{1/2}. \quad (17)$$

Results for  $R_F$  are presented in Fig. 10 for SFTs (Fig. 10a) and EFTs (Fig. 10b). For SFTs we see a clear general tendency for nondiffusive fluxes to become more important as conditions become more unstable, regardless of the version of the optimization. It is interesting to note, however, that nondiffusive

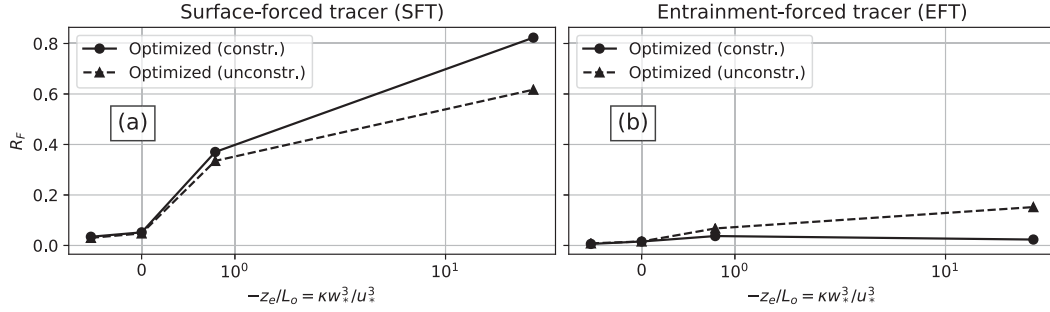


FIG. 10. Ratio of nondiffusive to total fluxes  $R_F$ , defined in Eq. (17). Solid black lines are results for the constrained optimization and dashed black lines are results for the unconstrained version. Results are shown for (a) SFTs and (b) EFTs. Note that the horizontal axis has a linear scale from  $-1$  to  $1$  and a log scale everywhere else for convenience.

fluxes are important even for weakly unstable conditions. For example, simulation Rolls ( $\kappa w_*^3/u_*^3 \approx 0.8$  in the figure) has  $R_F \approx 0.4$ , which indicates that about 40% of the flux is nondiffusive and the contribution of the nondiffusive fluxes reaches 80% for the constrained optimization in the most convective regime. It is worth noting that, due to possible cancellations among the flux components and an extra term in the denominator, interpreting  $R_F$  as a percentage of fluxes is not precisely correct. However, we take this as a reasonable approximation for simplicity.

In Fig. 10b we see results for EFTs, where there is a similar monotonically increasing tendency for the unconstrained version of the optimization. Note that the values of  $R_F$  for this are much lower than for SFTs, as expected. Constraining the optimization, however, does appear to qualitatively change results for EFTs, since there is no monotonic increase with stability in this case.

#### b. Modeling considerations

We begin by considering the modeling of the diffusive component of the total flux and analyze our eddy diffusivity estimates by some bulk measure. Taking a bulk mixing-length argument (Davidson 2004, section 4.1.2) and ignoring any coefficients which might be present, one may approximate  $K \sim z_e U_s$ , where  $U_s$  is a velocity scale of the flow relevant to the mixing. We can estimate  $U_s$  for our optimization-based estimate using the peak of  $K(z)$  in the ABL:

$$U_s^{\text{OPT}} = \frac{\text{MAX}[K^{\text{OPT}}(z)]}{z_e}, \quad (18)$$

where  $K^{\text{OPT}}$  refers to the eddy diffusivity results obtained with the optimization procedures. Introducing a similar bulk measure  $U_s^{\text{TM86}}$  for TM86's eddy diffusivities, we can create a measure  $R_U$  as

$$R_U = \frac{U_s^{\text{OPT}}}{U_s^{\text{TM86}}}. \quad (19)$$

Given that our optimization attempts to maximize  $K(z)$  based on data (and thus can be seen as an upper bound for  $K(z)$ ), a situation where  $R_U < 1$  implies that the classic TM86 parameterization predicts larger eddy diffusivities than are supported by data.

Results for  $R_U$  can be seen in Fig. 11 as a function of stability. Note that, for all cases,  $R_U \approx 1$  which indicates that TM86 curves do not overpredict  $K(z)$ , as expected. Moreover, TM86 estimates agree remarkably well with our optimized ones for the stable and neutral cases. In strongly convective conditions (simulation Plumes) the values for both optimizations are around  $R_U \approx 2$ , but since most of the flux is performed by  $F_{\text{ND}}$  (see Fig. 10) the precise value of  $K(z)$  is less important in this case.

The largest ratio  $R_U$  happens for the weakly unstable regime, where  $w_*/u_* = \mathcal{O}(1)$  and shear and buoyancy forcings are comparable. Although intermediate regimes are generally more challenging to capture, the large difference is somewhat surprising. Note that although we choose  $h$  in an ad hoc manner, our value is always within 10% of the canonical estimate for  $h$  and, at maximum, we are introducing a 10% error in  $U_s^{\text{TM86}}$  when compared to a more rigorous calculation of  $K^{\text{TM86}}$ .

In TM86's model  $U_s^{\text{TM86}}$  is associated with MO similarity theory due to the surface scaling [according to TM86,  $\text{MAX}(K) \approx 0.15 u_* h / \phi$ ]. Thus, this large value of  $R_U$  for simulation Rolls suggests that TM86's assumption that MO similarity theory determines  $K(z)$  in the bulk of the ABL may not be appropriate for weakly unstable conditions. From a physical

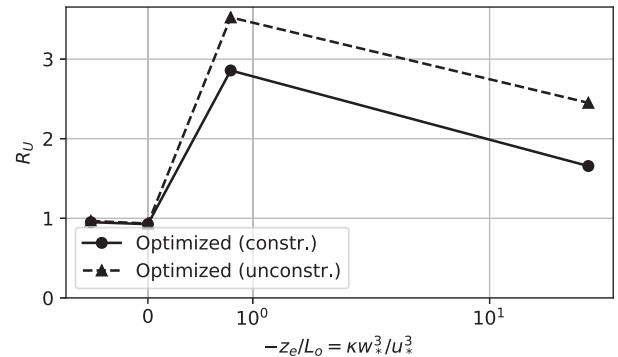


FIG. 11. Results for  $R_U$  using both versions of the optimization algorithm. Solid line shows results for the constrained optimization and dashed lines show results for the unconstrained version. Note that the horizontal axis has a linear scale from  $-1$  to  $1$  and a log scale everywhere else for convenience.

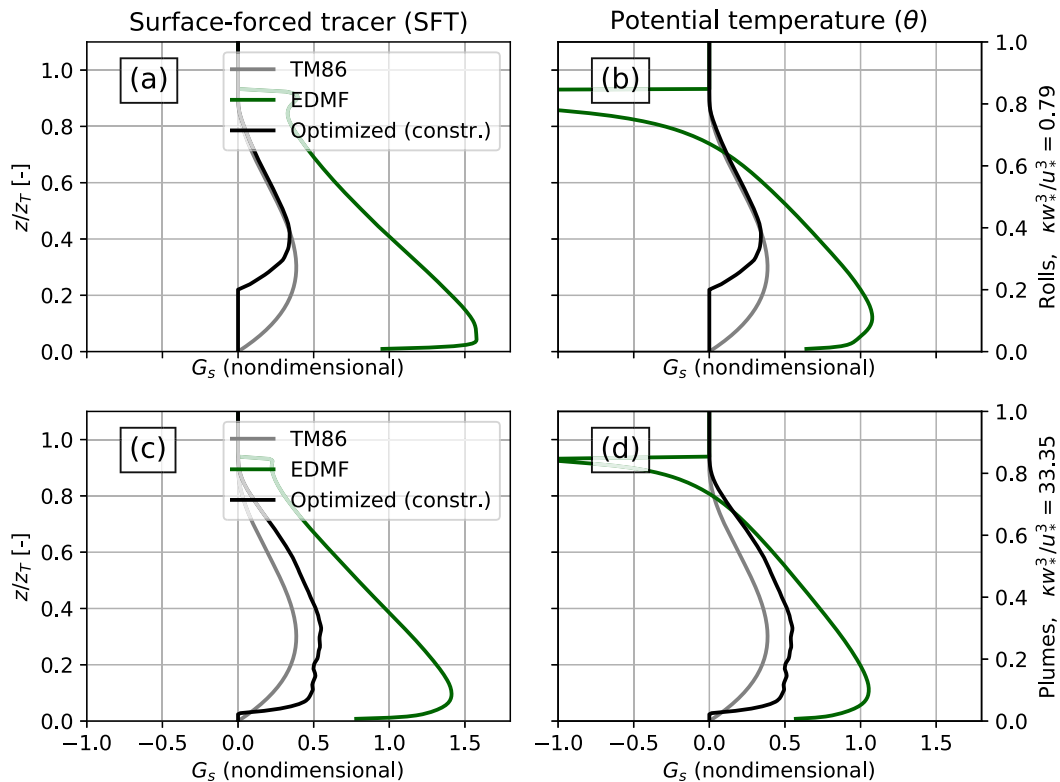


FIG. 12. Comparison of  $G_s$  between our constrained optimization (black line), TM86's model (gray line), and EDMF (green) for both unstable simulations in this work.  $G_s$  is calculated for TM86 and EDMF as (a),(c)  $F_{ND,SFT}/\langle w'c'_{SFT} \rangle_s$  and (b),(d)  $F_{ND,\theta}/\langle w'\theta' \rangle_s$ .

perspective, this points to the ABL being more diffusive than MO similarity theory would predict and further investigation would be helpful to clarify this issue. From a modeling perspective, there is an opportunity for improvement of TM86's model that could be implemented by making the bulk of the ABL independent from MO similarity theory and/or introducing a stability dependence on the shape function  $G$ .

Focusing now on the modeling of the nondiffusive component of the flux  $F_{ND}$ , we refer back to Figs. 9 and 10b.  $G_e$  profiles change between simulations Rolls and Plumes in a nontrivial way, making it challenging to model contributions from entrainment processes to  $F_{ND}$ . However, contributions from entrainment processes to nondiffusive fluxes are below 20% across the regimes considered in this work for EFTs and below 10% considering the constrained version of the optimization (Fig. 10b). This result justifies the community practice of neglecting nondiffusive contributions from entrainment processes (i.e.,  $G_e = 0$ ).

Furthermore, this motivates us to consider a truncated decomposition where  $G_e$  is neglected and we approximate  $F_{ND} \approx \langle w'c' \rangle_s G_s$ . Note that this is not the same as assuming  $G_e = 0$  and only then calculating  $K(z)$  and  $G_s$ . This latter approach is illustrated in the appendix and it produces unrealistic results for  $G_s$  near the surface. In our approach  $G_e$  is calculated alongside  $K(z)$  and  $G_s$  with our optimization procedure (thus using the same curves that were already presented) but is subsequently neglected, thus creating a truncated decomposition. This

allows us to use the estimated shape for  $G_s$  (already shown in the left panels of Fig. 9) as a guide to modeling.

To that end, we consider the two main currently used modeling approaches for  $G_s$  for qualitative comparison with our results: TM86's model and EDMF, whose profiles for  $G_s$  are calculated as  $G_s = F_{ND,SFT}/\langle w'c'_{SFT} \rangle_s$ . TM86's model is fully described by Eqs. (6)–(9). For EDMF's calculation of  $F_{ND}$  [given by Eq. (10)] we need expressions for the mass flux  $M$  and the tracer concentration in the updrafts  $\langle C \rangle_u$ . It is beyond the scope of the present work to compare different formulations for these quantities and we use Eqs. (7), (10), (17), (21), and (23) (along with respective constants) from Siebesma et al. (2007) to model  $M$  and  $\langle C \rangle_u$ . These equations are run diagnostically using LES profiles averaged over an hour as the environment average.

Figures 12a and 12c show  $G_s$  for simulations Rolls and Plumes according to our constrained optimization, TM86's model, and EDMF. TM86's model is qualitatively similar to our optimized curve, especially in the strongly unstable regime (Fig. 12c). The values of  $G_s$  from the EDMF model are unphysical in the sense that their magnitude is at times larger than unity in both simulations, indicating regions with larger fluxes than at the surface. This happens because we have performed a diagnostic analysis in which the EDMF calculations are carried out with averaged profiles from LES, rather than averaged profiles that are advanced in time using EDMF itself. This is due to the fact that our main goal is assessing the accuracy of

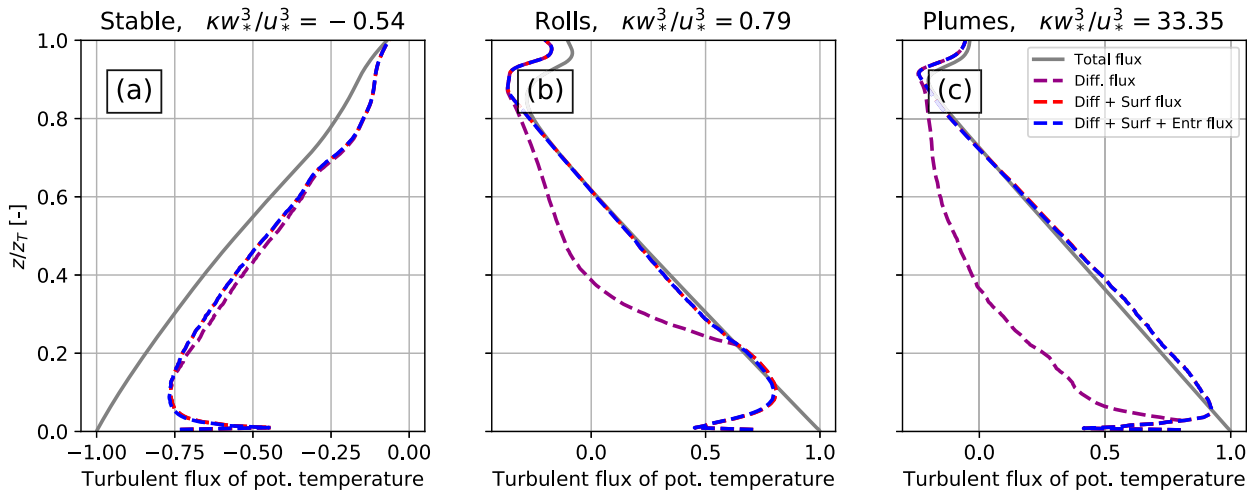


FIG. 13. Fluxes of potential temperature modeled with  $K(z)$ ,  $G_s$ , and  $G_e$  originally obtained for passive tracers. Results are shown for simulations (a) Stable, (b) Rolls, and (c) Plumes. Gray lines are average potential temperature fluxes from LES, purple lines are modeled fluxes using only a diffusive component, red lines include the diffusive component and the surface-driven nondiffusive component, and blue lines include all three components of Eq. (12). Ratios of temperature at entrainment vs surface  $\langle w'\theta' \rangle_e / \langle w'\theta' \rangle_s$  are 0.58,  $-0.18$ , and  $-0.14$  for simulations Stable, Rolls, and Plumes, respectively.

modeling assumptions rather than model performance after implementation (akin to an a priori test in LES literature; see Pope 2000, section 13.4.6; Meneveau and Katz 2000, section 2.1). Given that EDMF is built primarily as a prognostic tool, results are likely to improve if the averaged profiles used are also advanced in time using the EDMF model (Zhou et al. 2018), as is the case with most EDMF validations (Siebesma et al. 2007; Witek et al. 2011).

### c. Modeling of potential temperature fluxes

To further investigate results from EDMF, we calculate the shape of the nondiffusive contribution to the flux of potential temperature  $\theta$  via EDMF equations for simulations Rolls and Plumes, which are plotted in Figs. 12b and 12d. We also plot our optimized  $G_s$  (which is strictly only valid for passive scalars) in the same figure for comparison. Although there are regions where  $G_s \approx 1$  for temperature according to EDMF, EDMF profiles for  $\theta$  are more realistic than for SFTs. Furthermore, profiles are similar between simulations Rolls and Plumes, with the main difference being fluxes at entrainment, in which an unphysical result happens for simulation Rolls ( $G_s < -1$ ). Note that in our optimized decompositions and in TM86's model entrainment fluxes are almost fully a diffusive process, but the opposite is true for EDMF.

Although results for SFTs and temperature may signal a systematic inability of EDMF to represent regimes other than a purely convective one (i.e., free of mean shear), this is in contrast to its use in global models such as the European Centre for Medium-Range Weather Forecasts model (Köhler et al. 2011). This could be explained by the aforementioned differences between the diagnostic nature of our analyses and the prognostic nature of the implementations. Given the complexity of the EDMF model, further research is needed to evaluate these claims.

Although the obtained profiles for  $K(z)$ ,  $G_s$ , and  $G_e$  are only valid for passive tracers, we can assume their validity for potential temperature in order to assess the possible universality of such profiles. Note that there is no obvious reason to expect that the curves optimized for passive tracers should work well for temperature; however, such universality would be very convenient for modeling purposes and should be investigated. We examine this possibility by using  $K(z)$ ,  $G_s$ , and  $G_e$  profiles calculated from SFTs and EFTs with a constrained optimization to estimate potential temperature fluxes using Eq. (12) along with averaged profiles of temperature, temperature flux at entrainment  $\langle w'\theta' \rangle_e$  and at the surface  $\langle w'\theta' \rangle_s$  from LES. Results are shown in Fig. 13 for simulations Stable, Rolls, and Plumes. Each panel shows the measured flux from LES and three different modeling approaches with increasing number of terms. It is clear that the fluxes are better reproduced in the unstable simulations than in the Stable simulation. It is also clear that surface-driven nondiffusive fluxes are important to reconstruct the fluxes in the unstable cases, but entrainment-driven nondiffusive fluxes are not (as expected given the results in Fig. 10). For unstable simulations results using all three terms are remarkably close in most of the ABL but appear to diverge at the surface. Note that all places where there are significant discrepancies between modeled and LES results (the whole Stable ABL and in the surface layer of unstable cases) are marked by a dominance of diffusive fluxes. This implies that the difference between model and LES-measured fluxes can be accounted for by Prandtl and Schmidt numbers.

## 6. Conclusions

In this work we have introduced a framework for decomposing turbulent fluxes of passive scalars into diffusive ( $F_D$ ) and nondiffusive components ( $F_{ND}$ ). Our approach is of diagnostic nature and is based on a partition of the total flux



into three distinct terms and a subsequent optimization that estimates them simultaneously without any shape or scaling assumptions whatsoever. Our method requires two separate tracers to be present (an SFT and an EFT) and works in any stability regime. Its premise is to take as much advantage of diffusive fluxes as possible, thus maximizing the eddy diffusivity  $K(z)$ . Two versions of the method are introduced: while in the unconstrained version there are no restrictions to  $F_{ND}$ , in the constrained version we require that there be no counter-gradient fluxes for tracers with monotonically decreasing (or increasing) concentration profiles.

Application of our method to LESs reveals that, even when minimizing  $F_{ND}$ , nondiffusive fluxes are still important in ABLs that range from weakly to strongly unstable. Furthermore, in the constrained version of the optimization, the entrainment-forced nondiffusive transport (parameterized by  $G_e$ ) can be neglected and most of the nondiffusive fluxes are due to surface processes ( $G_s$ ). This justifies the widely adopted modeling practice of attributing all nondiffusive fluxes to surface-emerging coherent structures (plumes and rolls). However, the constrained optimization has the disadvantage of producing nondiffusive fluxes that are significant close to the surface for strongly convective cases (see Fig. 9g) where, according to MO similarity theory, we would expect all the flux to be diffusive. An interesting result from our decomposition is that, despite there being evidence that most of the turbulent fluxes in the entrainment layer of convective ABLs is accomplished by coherent plumes (Zhou et al. 2018), our results suggest that they can be fully modeled as a diffusive process.

Furthermore, qualitative comparison with currently used models showed that improvements are possible both in the calculation of  $F_D$  and of  $F_{ND}$ . Our results suggest that in weakly unstable regimes (where  $u_* \approx w_*$ ) models based on TM86 predict  $K(z)$  to be much smaller than our optimized  $K(z)$ , thus underutilizing diffusive fluxes. This indicates that the middle of the ABL is significantly more diffusive than TM86 model it to be. The reason for this feature is that in TM86-based models the magnitude of  $K(z)$  above the surface layer is set by MO similarity theory despite being outside its region of validity [see Eq. (6)]. Moreover, our results indicate that the shape of  $F_{ND}$  should vary with different stability conditions, which is currently not included in these models.

Finally, our optimization approach to estimate  $K(z)$  and  $F_{ND}$  can be useful for model building and assessment. As an assessment tool, our method can be used to identify situations where existing parameterizations are unrealistic, since it gives upper bounds for  $K(z)$  and lower bounds for  $F_{ND}$ . As a model-building tool, it can also be used to map  $K(z)$  and  $F_{ND}$  over a large number of stability conditions, thus providing modeling-optimized profiles for  $K(z)$ ,  $G_s$ , and  $G_e$  that should be valid throughout a wide range of stability regimes. Although in principle these profiles are strictly valid only for passive scalars, a reasonable modeling assumption would be that they can be extended for temperature, which was shown to produce reasonable results for unstable conditions (albeit with a possible need for Prandtl and Schmidt number considerations). Moreover, modifying our method by replacing the SFT with temperature yields very similar results, further building

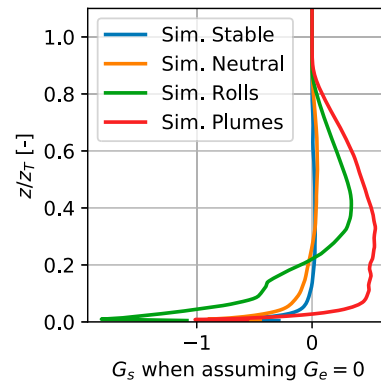


FIG. A1. Profiles for  $G_s$  when performing a two-term decomposition by assuming  $G_e = 0$ .

confidence in the extension for the temperature case. The extension for momentum may be more challenging since in many situations the vertical eddy viscosity has to be represented as a tensor.

**Acknowledgments.** This research was made possible by a grant from the Gulf of Mexico Research Initiative. We would like to acknowledge high-performance computing support from Cheyenne (doi:10.5065/D6RX99HX) provided by NCAR's Computational and Information Systems Laboratory, sponsored by the National Science Foundation.

**Data Availability Statement.** Data are publicly available through the Gulf of Mexico Research Initiative Information and Data Cooperative (GRIIDC) at <https://data.gulfresearchinitiative.org/data/R5.x283.000:0007> (doi:10.7266/SD6S0Y9M).

## APPENDIX

### Alternative Closures to Eqs. (13)–(15)

In this appendix we show why both currently used flux decompositions fail one of more of the plausibility criteria introduced in section 2, motivating the need for the broader decomposition given by Eq. (12).

The fully diffusive separation (and therefore WB84's model) violates criterion 1 since  $K(z)$  is different for SFTs and EFTs in convective ABLs (see Fig. 8) and can violate criterion 2 depending on the ratio  $\langle w'c' \rangle_e / \langle w'c' \rangle_s$  (Holtslag and Moeng 1991). Two-term separations can be arrived at by adding an extra equation to Eqs. (13) and (14). The most logical option is to assume  $G_e = 0$ , which makes physical sense and is in line with D66's model but violates criterion 3. Due to this violation, the  $G_s$  profile produced by this option exhibits a region close to the surface where  $G_s < 0$  (as shown in Fig. A1) where we would expect  $G_s \approx 0$  according to MO similarity theory. These negative values of  $G_s$  are large enough that they are understood as a qualitative deficiency of this approach.

Two other obvious alternatives exist, but are not appealing from a physical perspective and have no analogous in the literature. Assuming  $G_s = 0$  produces a situation where the only the nondiffusive fluxes are entrainment driven and, while this

does not violate any of our criteria, it is an undesirable characteristic for a decomposition. Finally, one can set  $G_s = G_e$ , which produces determined linear system of equation, but the results violate criterion 2 (not shown).

## REFERENCES

- Bou-Zeid, E., C. Meneveau, and M. Parlange, 2005: A scale-dependent Lagrangian dynamic model for large eddy simulation of complex turbulent flows. *Phys. Fluids*, **17**, 025105, <https://doi.org/10.1063/1.1839152>.
- Brasseur, J. G., and T. Wei, 2010: Designing large-eddy simulation of the turbulent boundary layer to capture law-of-the-wall scaling. *Phys. Fluids*, **22**, 021303, <https://doi.org/10.1063/1.3319073>.
- Chamecki, M., C. Meneveau, and M. B. Parlange, 2008: A hybrid spectral/finite-volume algorithm for large-eddy simulation of scalars in the atmospheric boundary layer. *Bound.-Layer Meteor.*, **128**, 473–484, <https://doi.org/10.1007/s10546-008-9302-1>.
- Chen, B., D. Yang, C. Meneveau, and M. Chamecki, 2016: Effects of swell on transport and dispersion of oil plumes within the ocean mixed layer. *J. Geophys. Res. Oceans*, **121**, 3564–3578, <https://doi.org/10.1002/2015JC011380>.
- Chinita, M. J., G. Matheou, and J. Teixeira, 2018: A joint probability density-based decomposition of turbulence in the atmospheric boundary layer. *Mon. Wea. Rev.*, **146**, 503–523, <https://doi.org/10.1175/MWR-D-17-0166.1>.
- Corrsin, S., 1975: Limitations of gradient transport models in random walks and in turbulence. *Advances in Geophysics*, Vol. 18, Elsevier, 25–60, [https://doi.org/10.1016/S0065-2687\(08\)60451-3](https://doi.org/10.1016/S0065-2687(08)60451-3).
- Davidson, P., 2004: *Turbulence: An Introduction for Scientists and Engineers*. Oxford University Press, 680 pp.
- Deardorff, J., 1966: The counter-gradient heat flux in the lower atmosphere and in the laboratory. *J. Atmos. Sci.*, **23**, 503–506, [https://doi.org/10.1175/1520-0469\(1966\)023<0503:TCGHFI>2.0.CO;2](https://doi.org/10.1175/1520-0469(1966)023<0503:TCGHFI>2.0.CO;2).
- Elliott, Z. A., and S. K. Venayagamoorthy, 2011: Evaluation of turbulent Prandtl (Schmidt) number parameterizations for stably stratified environmental flows. *Dyn. Atmos. Oceans*, **51**, 137–150, <https://doi.org/10.1016/j.dynatmoce.2011.02.003>.
- Fiedler, B. H., 1984: An integral closure model for the vertical turbulent flux of a scalar in a mixed layer. *J. Atmos. Sci.*, **41**, 674–680, [https://doi.org/10.1175/1520-0469\(1984\)041<0674:AICMFT>2.0.CO;2](https://doi.org/10.1175/1520-0469(1984)041<0674:AICMFT>2.0.CO;2).
- Ghannam, K., T. Duman, S. T. Salesky, M. Chamecki, and G. Katul, 2017: The non-local character of turbulence asymmetry in the convective atmospheric boundary layer. *Quart. J. Roy. Meteor. Soc.*, **143**, 494–507, <https://doi.org/10.1002/qj.2937>.
- Hamba, F., 1993: A modified first-order model for scalar diffusion in the convective boundary layer. *J. Atmos. Sci.*, **50**, 2800–2810, [https://doi.org/10.1175/1520-0469\(1993\)050<2800:AMFOMF>2.0.CO;2](https://doi.org/10.1175/1520-0469(1993)050<2800:AMFOMF>2.0.CO;2).
- Holtslag, A., and C.-H. Moeng, 1991: Eddy diffusivity and countergradient transport in the convective atmospheric boundary layer. *J. Atmos. Sci.*, **48**, 1690–1698, [https://doi.org/10.1175/1520-0469\(1991\)048<1690:EDACTI>2.0.CO;2](https://doi.org/10.1175/1520-0469(1991)048<1690:EDACTI>2.0.CO;2).
- Hunt, J. C. R., J. C. Kaimal, and J. E. Gaynor, 1988: Eddy structure in the convective boundary layer—New measurements and new concepts. *Quart. J. Roy. Meteor. Soc.*, **114**, 827–858, <https://doi.org/10.1256/SMSQJ.48201>.
- Jayaraman, B., and J. G. Brasseur, 2018: The surprising transition in atmospheric boundary layer turbulence structure from neutral to moderately convective stability states and mechanisms underlying large-scale rolls. arXiv, <https://arxiv.org/abs/1807.03336>.
- Kader, B., and A. Yaglom, 1990: Mean fields and fluctuation moments in unstably stratified turbulent boundary layers. *J. Fluid Mech.*, **212**, 637–662, <https://doi.org/10.1017/S0022112090002129>.
- Kaimal, J. C., and J. J. Finnigan, 1994: *Atmospheric Boundary Layer Flows: Their Structure and Measurement*. Oxford University Press, 289 pp.
- , J. C. Wyngaard, D. A. Haugen, O. R. Coté, Y. Izumi, S. J. Caughey, and C. J. Readings, 1976: Turbulence structure in the convective boundary layer. *J. Atmos. Sci.*, **33**, 2152–2169, [https://doi.org/10.1175/1520-0469\(1976\)033<2152:TSITCB>2.0.CO;2](https://doi.org/10.1175/1520-0469(1976)033<2152:TSITCB>2.0.CO;2).
- Katul, G. G., A. G. Konings, and A. Porporato, 2011: Mean velocity profile in a sheared and thermally stratified atmospheric boundary layer. *Phys. Rev. Lett.*, **107**, 268502, <https://doi.org/10.1103/physrevlett.107.268502>.
- Khanna, S., and J. G. Brasseur, 1997: Analysis of Monin–Obukhov similarity from large-eddy simulation. *J. Fluid Mech.*, **345**, 251–286, <https://doi.org/10.1017/S0022112097006277>.
- Köhler, M., M. Ahlgrim, and A. Beljaars, 2011: Unified treatment of dry convective and stratocumulus-topped boundary layers in the ECMWF model. *Quart. J. Roy. Meteor. Soc.*, **137**, 43–57, <https://doi.org/10.1002/qj.713>.
- Kumar, V., J. Kleissl, C. Meneveau, and M. B. Parlange, 2006: Large-eddy simulation of a diurnal cycle of the atmospheric boundary layer: Atmospheric stability and scaling issues. *Water Resour. Res.*, **42**, W06D09, <https://doi.org/10.1029/2005WR004651>.
- Large, W. G., J. C. McWilliams, and S. C. Doney, 1994: Oceanic vertical mixing: A review and a model with a nonlocal boundary layer parameterization. *Rev. Geophys.*, **32**, 363–403, <https://doi.org/10.1029/94RG01872>.
- Li, D., 2019: Turbulent Prandtl number in the atmospheric boundary layer—Where are we now? *Atmos. Res.*, **216**, 86–105, <https://doi.org/10.1016/j.atmosres.2018.09.015>.
- Meneveau, C., and J. Katz, 2000: Scale-invariance and turbulence models for large-eddy simulation. *Annu. Rev. Fluid Mech.*, **32**, 1–32, <https://doi.org/10.1146/annurev.fluid.32.1.1>.
- Moeng, C.-H., and P. P. Sullivan, 1994: A comparison of shear- and buoyancy-driven planetary boundary layer flows. *J. Atmos. Sci.*, **51**, 999–1022, [https://doi.org/10.1175/1520-0469\(1994\)051<0999:ACOSAB>2.0.CO;2](https://doi.org/10.1175/1520-0469(1994)051<0999:ACOSAB>2.0.CO;2).
- O'Brien, J. J., 1970: A note on the vertical structure of the eddy exchange coefficient in the planetary boundary layer. *J. Atmos. Sci.*, **27**, 1213–1215, [https://doi.org/10.1175/1520-0469\(1970\)027<1213:ANOTVS>2.0.CO;2](https://doi.org/10.1175/1520-0469(1970)027<1213:ANOTVS>2.0.CO;2).
- Pope, S., 2000: *Turbulent Flows*. Cambridge University Press, 728 pp.
- Porté-Agel, F., C. Meneveau, and M. B. Parlange, 2000: A scale-dependent dynamic model for large-eddy simulation: Application to a neutral atmospheric boundary layer. *J. Fluid Mech.*, **415**, 261–284, <https://doi.org/10.1017/S0022112000008776>.
- Prandtl, L., 1942: Bemerkungen zur theorie der freien turbulenz. *Z. Angew. Math. Mech.*, **22**, 241–243, <https://doi.org/10.1002/zamm.19420220502>.
- Salesky, S. T., M. Chamecki, and E. Bou-Zeid, 2017: On the nature of the transition between roll and cellular organization in the convective boundary layer. *Bound.-Layer Meteor.*, **163**, 41–68, <https://doi.org/10.1007/s10546-016-0220-3>.
- Siebesma, A. P., P. M. Soares, and J. Teixeira, 2007: A combined eddy-diffusivity mass-flux approach for the convective boundary layer. *J. Atmos. Sci.*, **64**, 1230–1248, <https://doi.org/10.1175/JAS3888.1>.

- Stull, R. B., 1988: *An Introduction to Boundary Layer Meteorology*. Kluwer Academic, 666 pp.
- , 1993: Review of non-local mixing in turbulent atmospheres: Transilient turbulence theory. *Bound.-Layer Meteor.*, **62**, 21–96, <https://doi.org/10.1007/BF00705546>.
- Troen, I., and L. Mahrt, 1986: A simple model of the atmospheric boundary layer; sensitivity to surface evaporation. *Bound.-Layer Meteor.*, **37**, 129–148, <https://doi.org/10.1007/BF00122760>.
- van Dop, H., and G. Verver, 2001: Countergradient transport revisited. *J. Atmos. Sci.*, **58**, 2240–2247, [https://doi.org/10.1175/1520-0469\(2001\)058<2240:CTR>2.0.CO;2](https://doi.org/10.1175/1520-0469(2001)058<2240:CTR>2.0.CO;2).
- Virtanen, P., and Coauthors, 2019: SciPy 1.0—Fundamental algorithms for scientific computing in Python. arXiv, <https://arxiv.org/abs/1907.10121>.
- Williams, A. G., and J. M. Hacker, 1993: Interactions between coherent eddies in the lower convective boundary layer. *Bound.-Layer Meteor.*, **64**, 55–74, <https://doi.org/10.1007/BF00705662>.
- Witek, M. L., J. Teixeira, and G. Matheou, 2011: An integrated TKE-based eddy diffusivity/mass flux boundary layer closure for the dry convective boundary layer. *J. Atmos. Sci.*, **68**, 1526–1540, <https://doi.org/10.1175/2011JAS3548.1>.
- Wyngaard, J. C., and R. A. Brost, 1984: Top-down and bottom-up diffusion of a scalar in the convective boundary layer. *J. Atmos. Sci.*, **41**, 102–112, [https://doi.org/10.1175/1520-0469\(1984\)041<0102:TDABUD>2.0.CO;2](https://doi.org/10.1175/1520-0469(1984)041<0102:TDABUD>2.0.CO;2).
- , and J. C. Weil, 1991: Transport asymmetry in skewed turbulence. *Phys. Fluids*, **3A**, 155–162, <https://doi.org/10.1063/1.857874>.
- Zhou, B., S. Sun, K. Yao, and K. Zhu, 2018: Reexamining the gradient and countergradient representation of the local and non-local heat fluxes in the convective boundary layer. *J. Atmos. Sci.*, **75**, 2317–2336, <https://doi.org/10.1175/JAS-D-17-0198.1>.